Supporting Information

Fast Deposition of Ultrathin, Highly Crystalline Organic Semiconductor Film for High-Performance Transistors

Xiali Zhang, Wei Deng*, Bei Lu, Xiaochen Fang, Xiujuan Zhang, and Jiansheng Jie*

Institute of Functional Nano & Soft Materials (FUNSOM), Jiangsu Key Laboratory for Carbon-Based Functional Materials & Devices, Soochow University, Suzhou Jiangsu 215123, China

Table S1. Comparison of deposition speed of the ultrathin Dif-TES-ADT crystalline film in this work with other ultrathin OSC crystalline films fabricated in the literatures.

Material	Thickness (nm)	Speed (mm s^{-1})	Temperature (^{o}C)	Ref.
Dif-TES-ADT	**4.53 nm**	**1**	**50**	**This work**
C10-DNTT	4 nm	0.03	85-90	1
C8-DNBDT-NW	7.2 nm	0.02	60-62	2
Ph-BTBT-C10/Ph-BTBT-C6	4.4 nm	0.0025	Room temperature	3

References

1. Peng, B.; Huang, S.; Zhou, Z.; Chan, P. K. L., *Adv. Funct. Mater.* 2017**, 27**, 1700999.
2. Yamamura, A.; Watanabe, S.; Uno, M.; Mitani, M.; Mitsui, C.; Tsurumi, J.; Isahaya, N.; Kanaoka, Y.; Okamoto, T.; Takeya, J., *Sci. Adv.* 2018**, 4**, eaao5758.
3. Arai, S.; Inoue, S.; Hamai, T.; Kumai, R.; Hasegawa, T., *Adv. Mater.* 2018**, 30**, 1707256.

Table S2. Properties of solvents.

Solvents	**Surface tension @50℃ [mN·m^{-1}]**	**Boiling point [℃]**
m-xylene	25.71	139
o-DCB	32.57	180
2-chlorophenol	36.89	175
Iodobenzene	35.91	188

The surface tensions at 50°C were obtained from *CRC Handbook of Chemistry and Physics* (David, R. Lide, *CRC Handbook of chemistry and physics 84th edition*, 2003).

Table S3. Comparison of mobilities of the ultrathin Dif-TES-ADT crystalline film-based OTFTs in this work with Dif-TES-ADT film-based devices in the literature.

Material	Structure	Method	Mobility ($cm^2 V^{-1} s^{-1}$)	Ref.
Dif-TES-ADT	**Ultrathin film**	**Blade coating**	**5.54**	**Our work**
Dif-TES-ADT	Single crystal	PVD	6	1
Dif-TES-ADT	Film	Spray deposition	0.2	2
Dif-TES-ADT	Film	Drop casting	0.41	3
Dif-TES-ADT	Film	Drop casting	3	4
Dif-TES-ADT	Film	Spin coating	1.5	5
Dif-TES-ADT	Film	Spin coating	0.1-0.2	6
Dif-TES-ADT	Film	Spin coating	0.7	7
Dif-TES-ADT: PTAA	Film	Blade coating	0.31	8
Dif-TES-ADT: PαMS	Film	Blade coating	3.6	9
Dif-TES-ADT: PS	Film	Blade coating	1.9	10
Dif-TES-ADT: PS	Film	Blade coating	0.1	11
Dif-TES-ADT: PTAA	Film	Spin coating	2	12
Dif-TES-ADT: PTAA	Film	Spin coating	2.4	13
Dif-TES-ADT: PS/PαMS/PMMA	Film	Spin coating	0.09	14
Dif-TES-ADT: PTAA/PF-TAA	Film	Spin coating	5	15
Dif-TES-ADT: PTAA	Film	Spin coating	2.4	16
Dif-TES-ADT: PTAA	Film	Spin coating	0.1	17

References

1. Jurchescu, O. D.; Subramanian, S.; Kline, R. J.; Hudson, S. D.; Anthony, J. E.; Jackson, T. N.; Gundlach, D. J., *Chem. Mater.* 2008**, 20**, 6733.
2. Azarova, N. A.; Owen, J. W.; McLellan, C. A.; Grimminger, M. A.; Chapman, E. K.; Anthony, J. E.; Jurchescu, O. D., *Org. Electron.* 2010**, 11**, 1960.
3. Pitsalidis, C.; Pappa, A.-M.; Hunter, S.; Payne, M. M.; Anthony, J. E.; Anthopoulos, T. D.; Logothetidis, S., *ACS Appl. Mater. Interfaces* 2015**, 7**, 6496.
4. Diemer, P. J.; Lyle, C. R.; Mei, Y.; Sutton, C.; Payne, M. M.; Anthony, J. E.; Coropceanu, V.; Brédas, J. L.; Jurchescu, O. D., *Adv. Mater.* 2013**, 25**, 6956.
5. Park, S. K.; Mourey, D. A.; Subramanian, S.; Anthony, J. E.; Jackson, T. N., *Appl. Phys. Lett.* 2008**, 93**, 274.
6. Park, S. K.; Mourey, D. A.; Subramanian, S.; Anthony, J. E.; Jackson, T. N., *IEEE Electron Device Lett.* 2008**, 29**, 1004.
7. Subramanian, S.; Park, S. K.; Parkin, S. R.; Podzorov, V.; Jackson, T. N.; Anthony, J. E., *J. Am. Chem. Soc.* 2008**, 130**, 2706.
8. Pierre, A.; Sadeghi, M.; Payne, M. M.; Facchetti, A.; Anthony, J. E.; Arias, A. C., *Adv. Mater.* 2014**, 26**, 5722.
9. Niazi, M. R.; Li, R.; Abdelsamie, M.; Zhao, K.; Anjum, D. H.; Payne, M. M.; Anthony, J.; Smilgies, D. M.; Amassian, A., *Adv. Funct. Mater.* 2016**, 26**, 2371.
10. Temiño, I.; Del Pozo, F. G.; Ajayakumar, M.; Galindo, S.; Puigdollers, J.; Mas-Torrent, M., *Adv. Mater. Technol.* 2016**, 1**, 1600090.
11. Zhang, Q.; Leonardi, F.; Casalini, S.; Temiño, I.; Mas-Torrent, M., *Sci. Rep.* 2016**, 6**, 39623.

12. Zhao, K.; Wodo, O.; Ren, D.; Khan, H. U.; Niazi, M. R.; Hu, H.; Abdelsamie, M.; Li, R.; Li, E. Q.; Yu, L., *Adv. Funct. Mater.* 2016**, 26**, 1737.
13. Hunter, S.; Chen, J.; Anthopoulos, T. D., *Adv. Funct. Mater.* 2014**, 24**, 5969.
14. Shin, N.; Kang, J.; Richter, L. J.; Prabhu, V. M.; Kline, R. J.; Fischer, D. A.; DeLongchamp, D. M.; Toney, M. F.; Satija, S. K.; Gundlach, D. J., *Adv. Funct. Mater.* 2013**, 23**, 366.
15. Smith, J.; Zhang, W.; Sougrat, R.; Zhao, K.; Li, R.; Cha, D.; Amassian, A.; Heeney, M.; McCulloch, I.; Anthopoulos, T. D., *Adv. Mater.* 2012**, 24**, 2441.
16. Hamilton, R.; Smith, J.; Ogier, S.; Heeney, M.; Anthony, J. E.; McCulloch, I.; Veres, J.; Bradley, D. D.; Anthopoulos, T. D., *Adv. Mater.* 2009**, 21**, 1166.
17. Smith, J.; Hamilton, R.; Heeney, M.; de Leeuw, D. M.; Cantatore, E.; Anthony, J. E.; McCulloch, I.; Bradley, D. D.; Anthopoulos, T. D., *Appl. Phys. Lett.* 2008**, 93**, 448.

COMSOL Simulations

To simulate the fluid behavior in the solvent during the meniscus-guided coating process, we use a 2D model that takes into account fluid flow and heat transfer in the fluid domain. Assuming that the shearing process was at a quasi-equilibrium state, we considered the shape of the meniscus was unchanged during deposition and used a stationary model. The governing equations are shown below.

Laminar Flow

The solvent in this case was modeled by using incompressible Navier-Stokes equations:

$$\rho\left(\frac{\partial u}{\partial t} + (u \cdot \nabla)u\right) - \mu\nabla^2 u = -\nabla p + F$$

$$\nabla \cdot u = 0$$

where u = (u, v) represents the velocity vector of the solvent (m s^{-1}), μ represents the viscosity (Ns m^{-2}), ρ is the density (kg m^{-3}) and p is the pressure (Pa). F donates the force field which includes the gravity and the surface tension force acting at the liquid-gas interface. A non-slip condition was applied to the substrate and a slip condition was set to the interface.

Heat Transfer in Fluids

The heat transfer was described as:

$$\rho C_p u \cdot \nabla T = k\nabla^2 T$$

Here, $C_p$is the heat capacity (J kg^{-1} K^{-1}), k is the thermal conductivity, T is the temperature and **u** = (u, v) is the velocity vector of the solvent (m s^{-1}) which could be coupled with the velocity in Navier-Stokes equations. The temperature on the substrate is set as 323K and the initial temperature is set as ambient temperature.

Marangoni Flow

Since the equivalent size is small, the surface tension of the interface depends on the temperature distribution and then the Marangoni effect occurs. It is described by the following contribution:

$$\left[-pI + \mu\left(\nabla u + (\nabla u)^T\right) - \frac{2}{3}\mu(\nabla \cdot u)I\right]n = \gamma\nabla_t T$$

Here, γ represents the temperature derivative of the surface tension which is 0.10836 (N m^{-1} K^{-1}) in this case. The Marangoni flow is coupled with heat transfer and fluid flow.

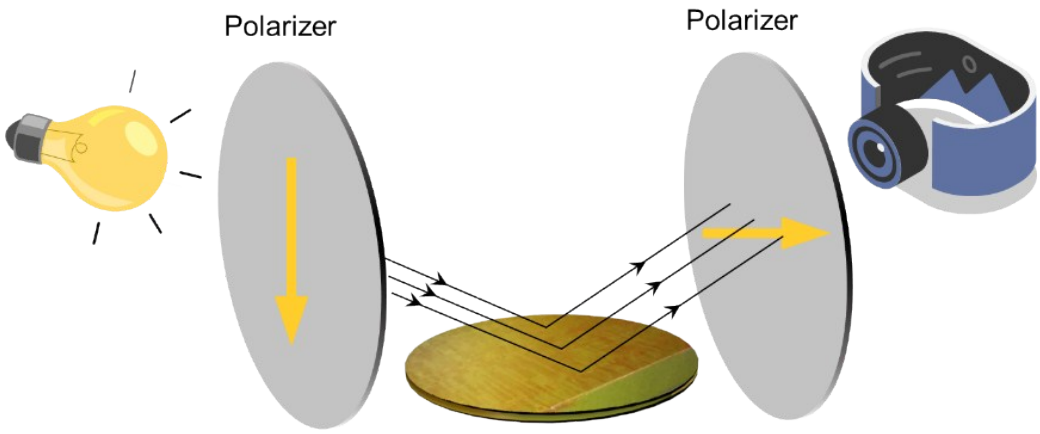

Fig. S1. Schematic diagram of the observation setup.

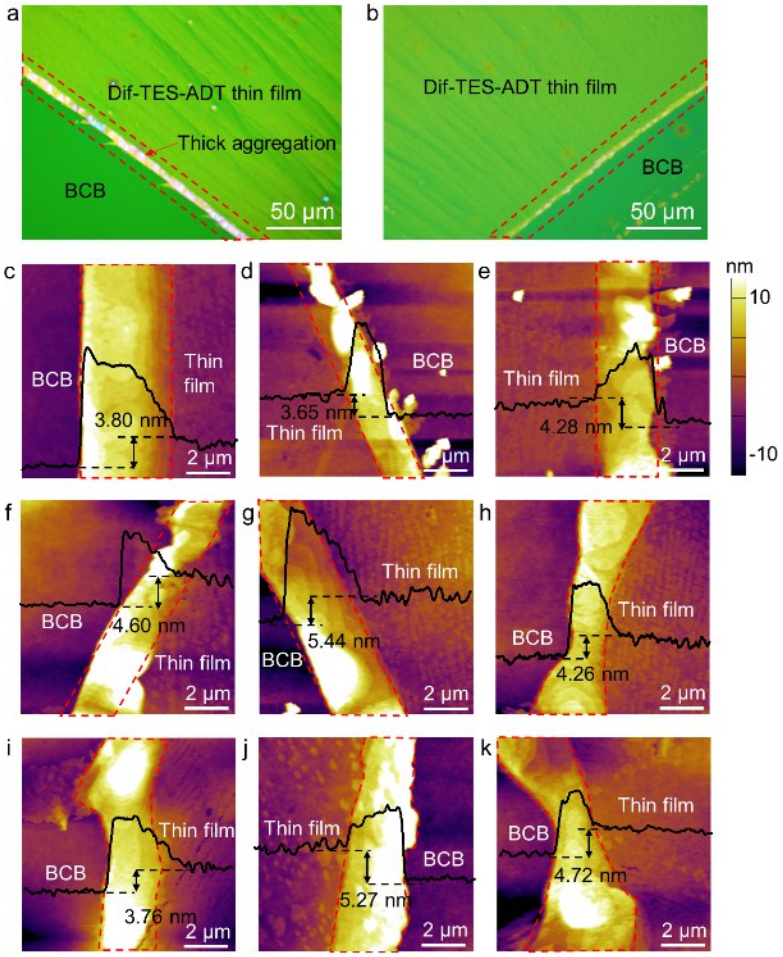

Fig. S2. (a, b) CPOM images of the Dif-TES-ADT crystalline film after partially removing the film using dichloromethane. Due to the coffee-ring effect, a thick aggregation of residues at the boundary of Dif-TES-ADT thin film was observed. (c-k) AFM images of the boundaries between the Dif-TES-ADT thin films and BCB substrates.

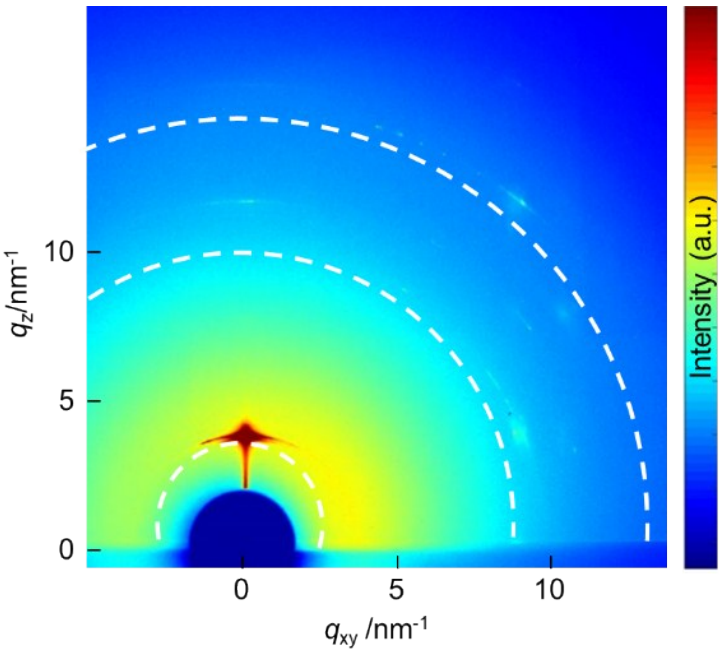

Fig. S3. 2D-GIXRD characterization of the spin-coated polycrystalline film, showing diffuse intensities around the (00l) diffraction peaks along with the Debye rings.

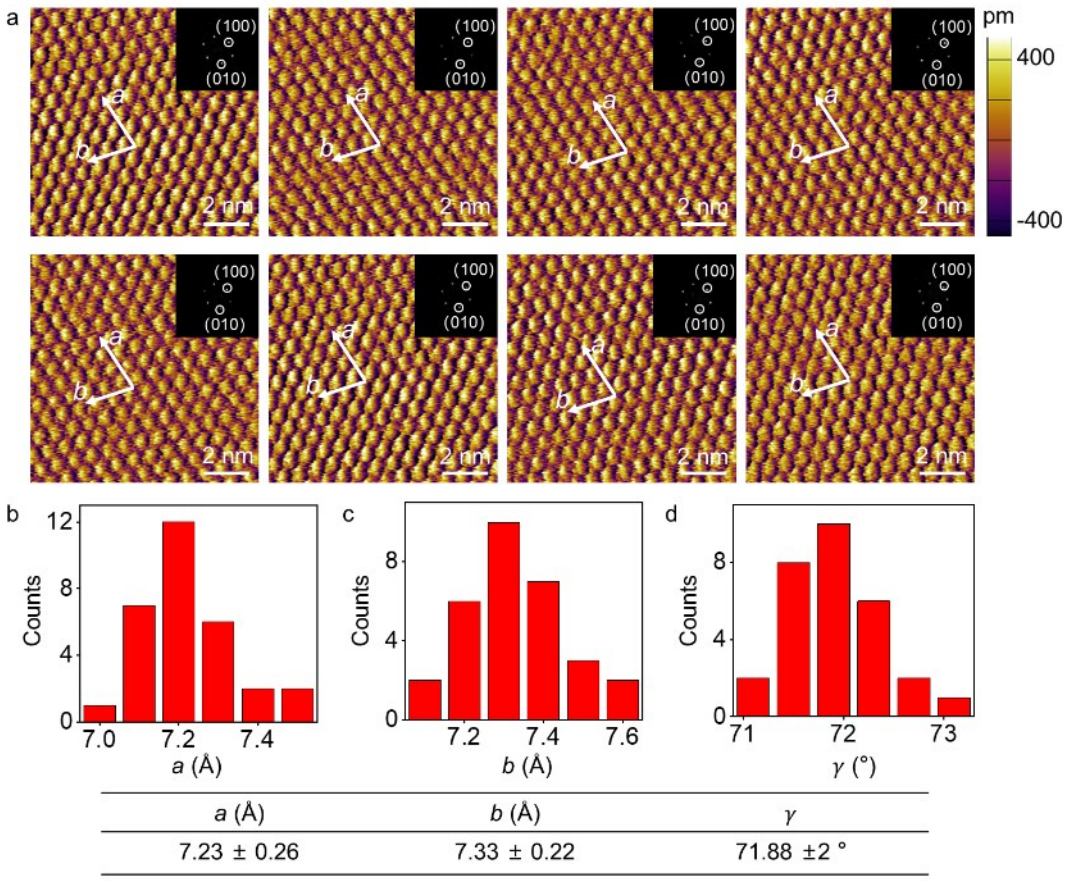

a (Å)	*b* (Å)	*γ*
7.23 ± 0.26	7.33 ± 0.22	71.88 ±2 °

Fig. S4. (a) HR-AFM images of the ultrathin Dif-TES-ADT crystalline film and their corresponding FFT patterns. (b-d) Histograms of lattice constants of the obtained ultrathin Dif-TES-ADT crystalline film extracted from the FFT patterns.

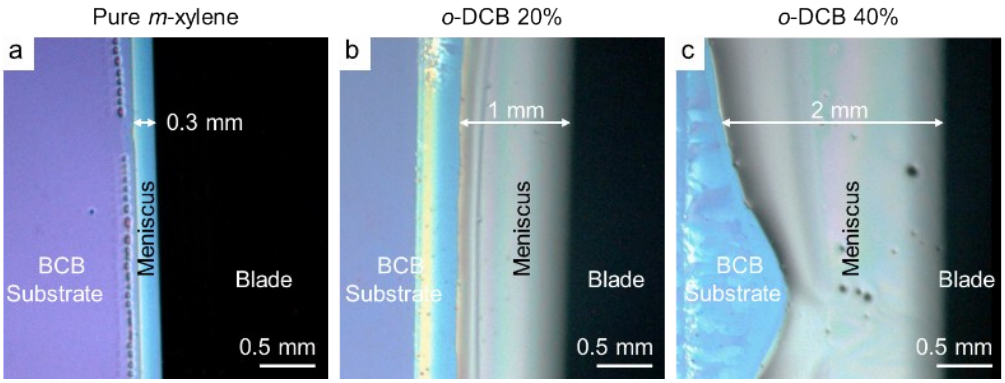

Fig. S5. Captured images from the top of the meniscus during blade coating. As the *o*-DCB concentration increases, the meniscus length increases. Blade-coating speed for all captures is 1 mm s^{-1}.

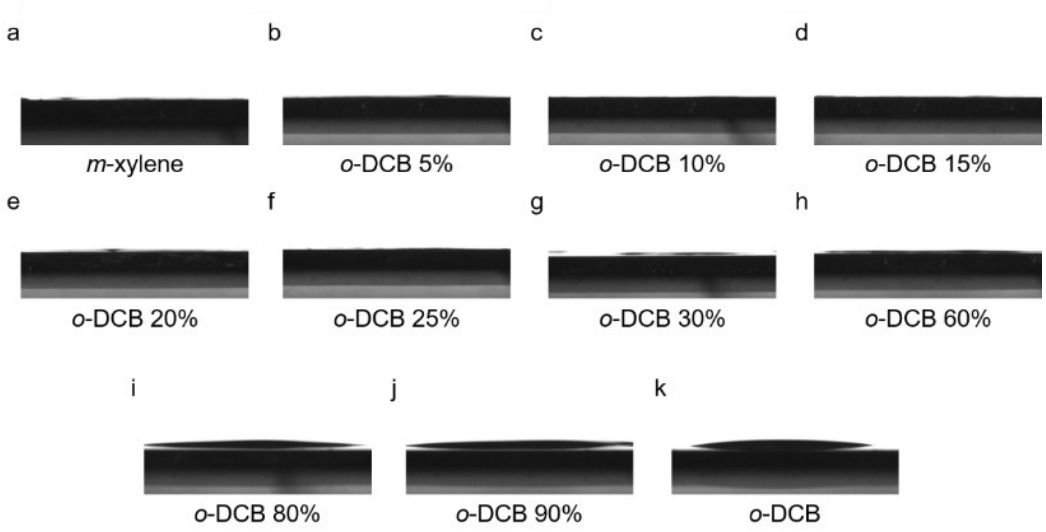

Fig. S6. (a-k) Contact angles of *m*-xylene, *o*-DCB, and the mixed solvents with different *o*-DCB concentrations on the BCB surface.

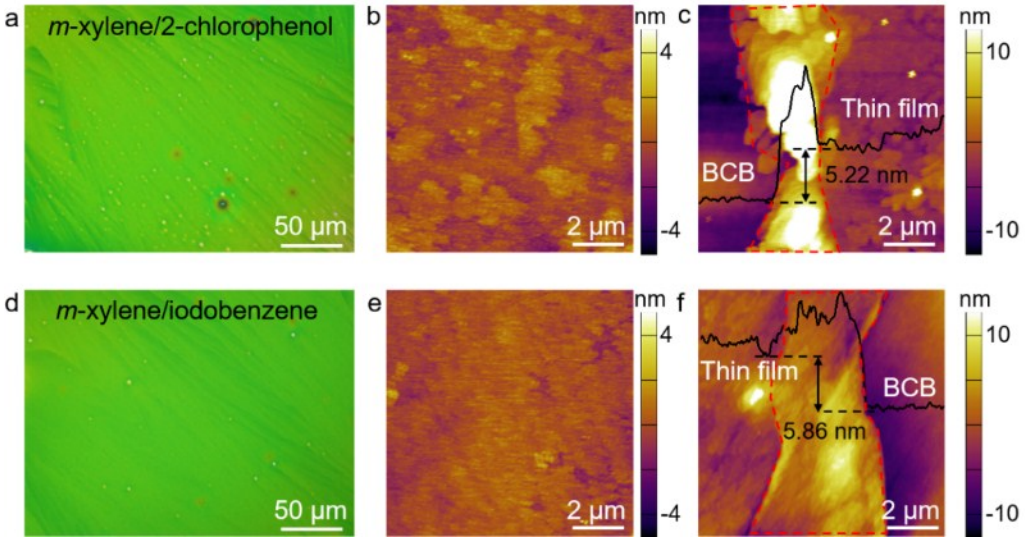

Fig. S7. CPOM and AFM images of the ultrathin Dif-TES-ADT films obtained from the mixed solvents of (a-c) *m*-xylene/2-chlorophenol and (d-f) *m*-xylene/iodobenzene, respectively.

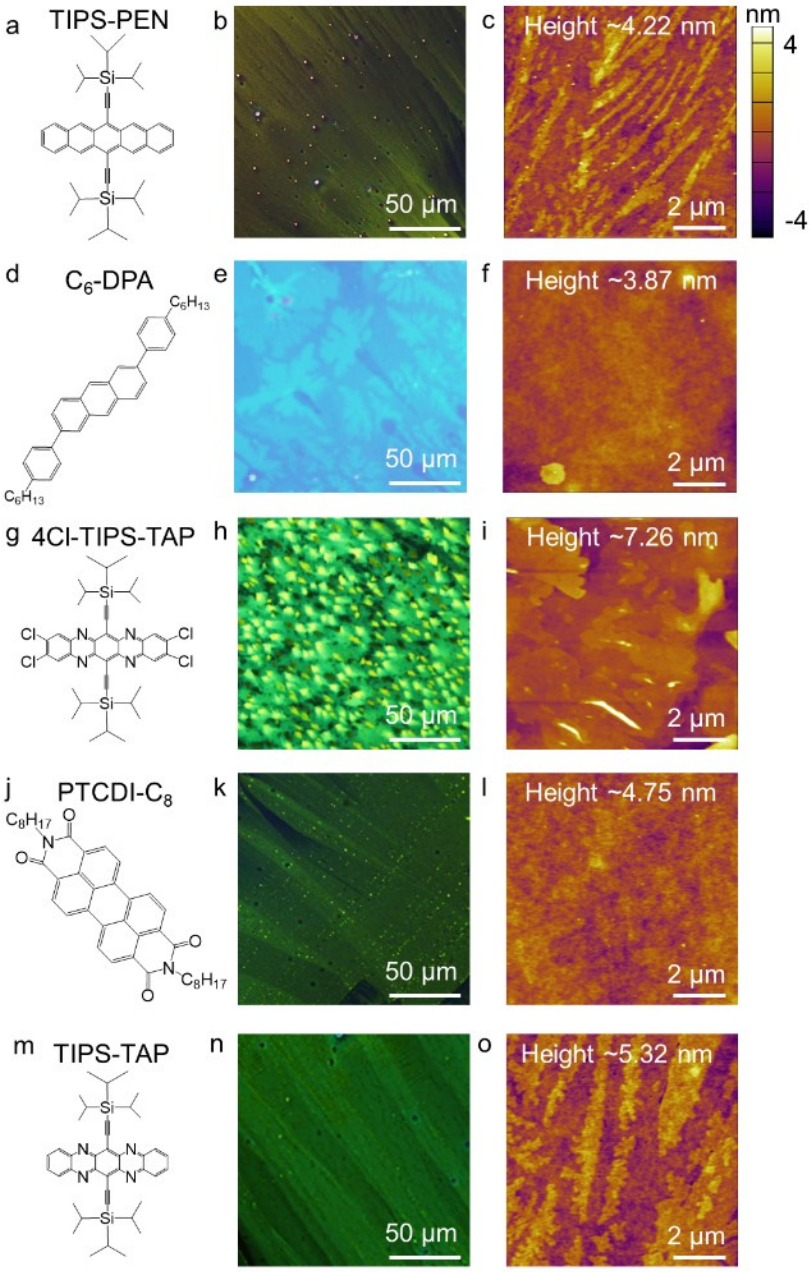

Fig. S8. Molecular structures of (a) TIPS-PEN, (d) C_6-DPA, (g) 4Cl-TIPS-TAP, (j) PTCDI-C_8, and (m) TIPS-TAP. (b-o) CPOM and AFM images of the corresponding ultrathin crystalline films.

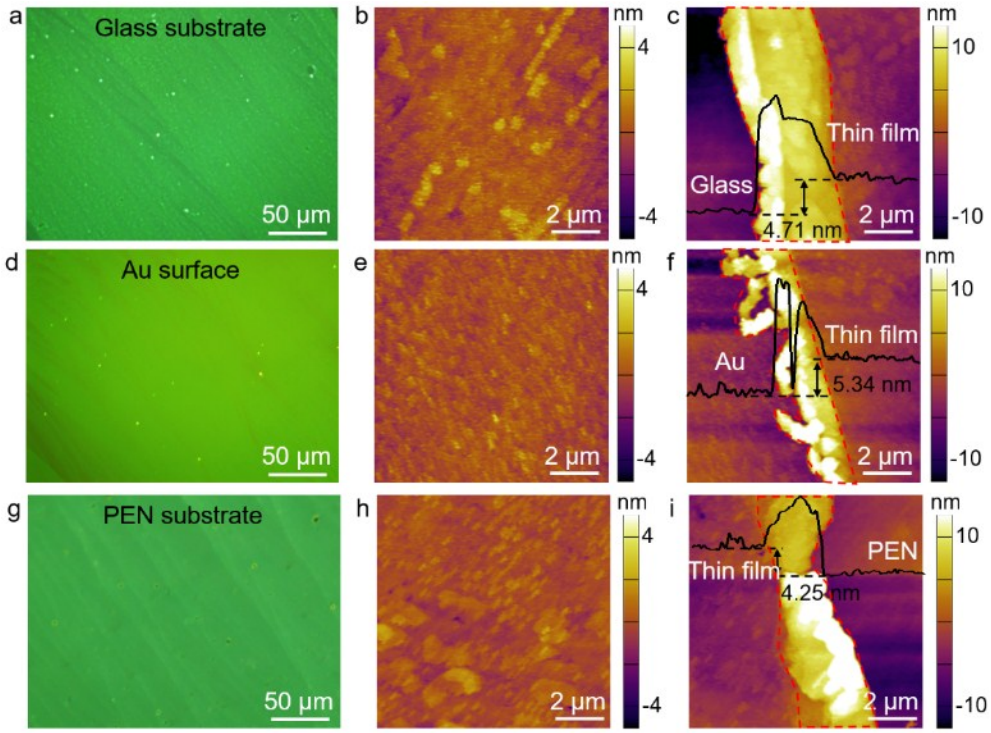

Fig. S9. CPOM and AFM images of the ultrathin Dif-TES-ADT films prepared on (a-c) glass substrate, (d-f) Au surface, and (g-i) PEN substrate, respectively.

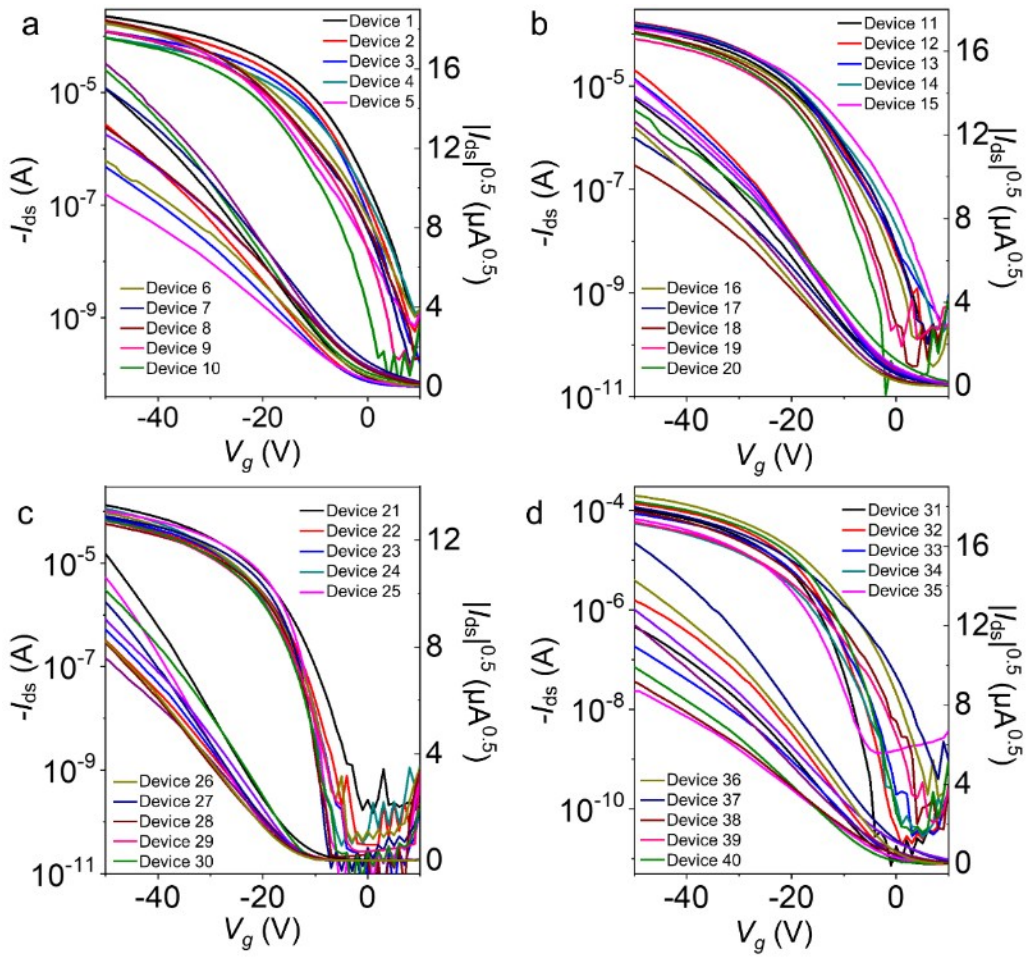

Fig. S10. (a-d) Transfer curves of the array of 5 × 8 ultrathin Dif-TES-ADT crystalline film-based OTFTs included in Fig. 6d.

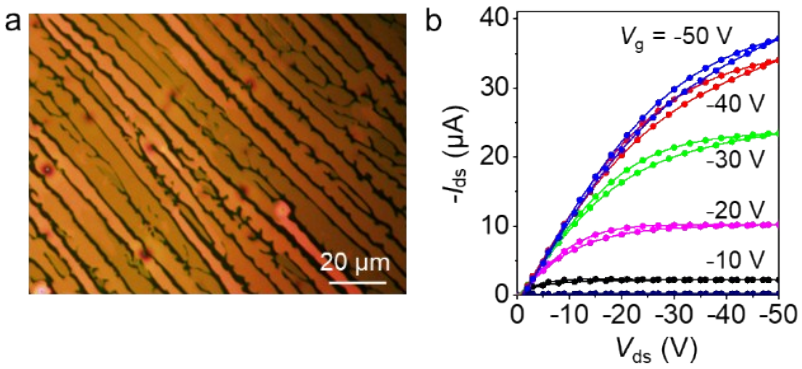

Fig. S11. (a) CPOM image and (b) output characteristics curve of the Dif-TES-ADT film fabricated from pure *m*-xylene solvent under an optimal blade-coating speed of ~0.3 mm s^{-1}.

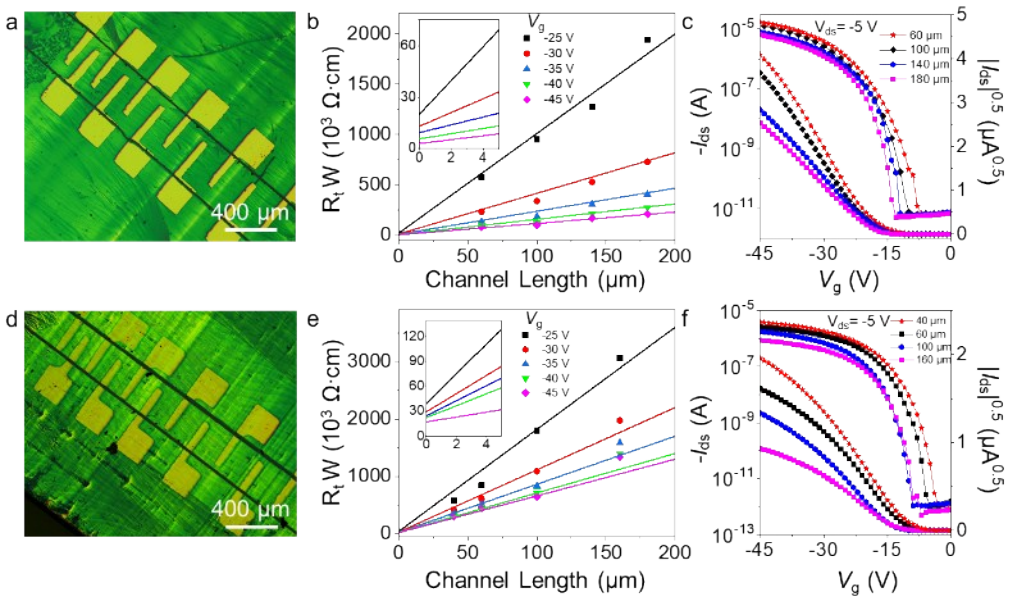

Fig. S12. (a) CPOM images of the ultrathin Dif-TES-ADT crystalline film-based OTFTs with different channel lengths. (b) R_tW of the ultrathin Dif-TES-ADT crystalline film-based OTFTs as a function of channel length at various gate bias. (c) Linear transfer curves in TLM measurement of the ultrathin Dif-TES-ADT crystalline film. (d) CPOM images of the Dif-TES-ADT film from pure *m*-xylene solvent-based OTFTs with different channel lengths. (e) R_tW of the Dif-TES-ADT film from pure *m*-xylene solvent -based OTFTs as a function of channel length at various gate bias. (f) Linear transfer curves in TLM measurement of Dif-TES-ADT film fabricated from pure *m*-xylene solvent.

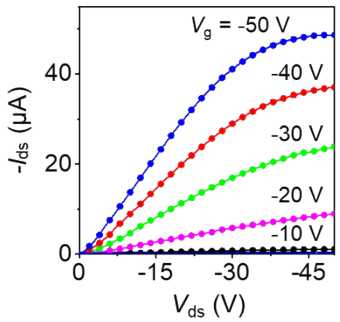

Fig. S13. Typical output characteristics of OFET base on the ultrathin Dif-TES-ADT crystalline film on the flexible substrate.

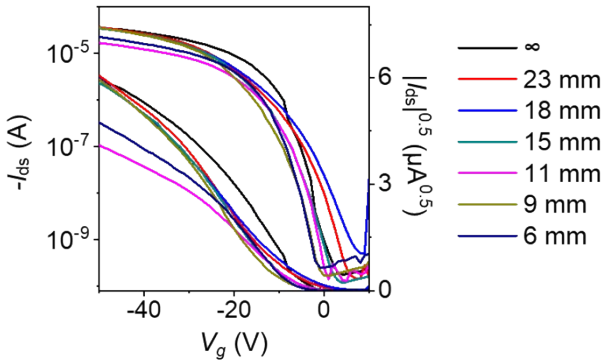

Fig. S14. Transfer curves of the ultrathin Dif-TES-ADT crystalline film-based OTFT under different bending radii.

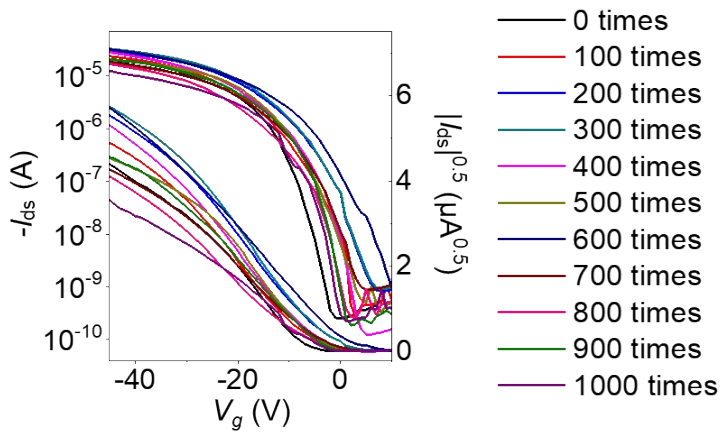

Fig. S15. Transfer curves of the ultrathin Dif-TES-ADT crystalline film-based OTFT under different bending times at a small bending radius of 6 mm.